

Crystal-plastic deformation of carbonate fault rocks through the seismic cycle

Markus Ohl¹, Billy Nzogang², Alexandre Mussi²,

David Wallis^{1†}, Martyn Drury¹, Oliver Plümper¹

¹ *Department of Earth Sciences, Utrecht University, Princetonlaan 8a, 3584 CB, Utrecht, The Netherlands*

² *Univ. Lille, CNRS, INRAE, ENSCL, UMR 8207 - UMET - Unité Matériaux et Transformations, F-59000 Lille, France*

Corresponding author: Markus Ohl (m.ohl@uu.nl)

[†]Present address: Department of Earth Sciences, University of Cambridge, Downing Street, Cambridge, CB2 3EQ, U.K.

Key points:

- Crystal-plastic deformation in seismically deformed carbonate rocks
- Deformation and annealing produce a grain-boundary strengthening effect
- Cyclic repetition of deformation and annealing leads to formation of multiple fault planes

27 Abstract

28 Detailed microstructural investigations of naturally deformed carbonate rocks are of interest for
29 unravelling potential co-seismic deformation mechanisms. The spatial separation of macroscopic
30 rheological behaviours has led to independent conceptual treatments of frictional failure, often
31 referred to as brittle, and viscous deformation. Here, we investigate the deformation mechanisms
32 that were active in two carbonate fault zones in Greece by performing detailed slip-system
33 analyses on data from automated crystal-orientation mapping transmission electron microscopy
34 and electron backscatter diffraction. We combine the slip system analyses with interpretations of
35 nanostructures and predictions from deformation mechanism maps for calcite. The nanometric
36 grains at the principal slip surface should deform by diffusion creep but the activation of the
37 $(0001)\langle\bar{1}2\bar{1}0\rangle$ slip system is evidence for a contribution of crystal plasticity. A similar
38 crystallographic preferred orientation appears in the cataclastic region of the fault rock despite
39 exhibiting a larger grain size and a different fractal dimension compared to the principal slip
40 surface. The cataclastic region exhibits microstructures consistent with activation of the
41 $(0001)\langle\bar{1}2\bar{1}0\rangle$ and $\{10\bar{1}4\}\langle\bar{2}021\rangle$ slip systems. Post-deformational, static recrystallisation and
42 annealing produces an equilibrium microstructure with triple junctions and equant grain size. We
43 propose a cyclic repetition of plastic strain and annealing, which reduces the grain size and offers
44 an alternative mechanism to form a cohesive nanogranular material. This mechanism leads to a
45 grain-boundary strengthening effect resulting in slip delocalisation which is observed over six
46 orders of magnitude (μm – m) and is expressed by multiple faults planes, suggesting cyclic
47 repetition of deformation and annealing over the seismic cycle.

48

49 1 Introduction

50 Seismic slip and aseismic creep often occur in distinct portions of the lithosphere due to
51 the different dependencies of the underlying deformation mechanisms on conditions such as
52 pressure and temperature (Scholz, 1998). Frictional failure involves dilatant processes facilitated
53 by low confining pressures at shallow depths (Sammis *et al.*, 1987; Sammis and Ben-Zion,
54 2008), whereas viscous deformation occurs by thermally activated processes promoted by higher
55 temperatures at greater depths (Sibson, 1982; Bürgmann and Dresen, 2008). However, the
56 temperature increase through shear heating during seismic faulting (Rice, 2006) challenges this
57 strict separation by potentially activating temperature-dependent deformation mechanisms, such
58 as crystal plasticity and diffusion creep (Nielsen, 2017). Depending on the material, melting or
59 decomposition reactions can also occur at high temperatures, leading to severe microphysical
60 changes that alter the mechanical behaviour of faults (Di Toro *et al.*, 2011; Niemeijer *et al.*,
61 2012). The main factor limiting the operation of crystal plasticity in the brittle regime is the
62 extremely short duration of the temperature increase during and after fault slip. Thermal models
63 predict a temperature drop through thermal diffusion within one second, after sliding ceased, to a
64 value similar to the background temperature (Demurtas *et al.*, 2019). Therefore, a key objective
65 of earthquake geology is to assess the extent to which thermally activated processes impact fault
66 structure and properties during the short interval of the coseismic temperature spike.

67 Deformed carbonates from principal slip zones of natural and experimental faults often
68 exhibit crystallographic preferred orientations (CPOs) (Smith *et al.*, 2013; Verberne *et al.*, 2013;
69 Delle Piane *et al.*, 2017; Kim *et al.*, 2018; Demurtas *et al.*, 2019; Pozzi *et al.*, 2019). Most of the
70 CPOs involve (0001) planes aligned subparallel to the shear plane, typically with an antithetic
71 inclination against the shear direction. In addition, the CPOs include alignment of the $\langle\bar{1}2\bar{1}0\rangle$
72 axes subparallel to the shear direction. Similar CPOs are generated in high-temperature, low-

73 strain rate experiments, in which calcite is deformed by dislocation-mediated deformation
74 mechanisms (Pieri *et al.*, 2001). In general, the observations of CPOs in carbonate fault rocks
75 suggest that crystal plasticity may play a role during seismic deformation. The contrast between
76 frictional failure at the macroscale and the formation of CPOs by dislocation-mediated processes
77 at the microscale demonstrates the need to further constrain the spatial and temporal evolution of
78 deformation mechanisms during fault slip.

79 At the microscale, high-temperature grain-boundary sliding (GBS) has been suggested to
80 operate within the gouge volume near the principal slip surface (PSS) (De Paola *et al.*, 2015). In
81 the pursuit of predicting rheological behaviour during seismic fault slip, De Paola *et al.* (2015)
82 used deformation mechanism maps constructed from steady-state flow laws. Specifically for
83 carbonates with small grain sizes, these flow laws predict the operation of grain-size sensitive
84 (GSS) deformation mechanisms such as diffusion creep (Herwegh *et al.*, 2003) and dislocation-
85 accommodated grain boundary sliding (disGBS) (Walker *et al.*, 1990). In contrast, coarse-
86 grained carbonates are predicted to exhibit grain-size insensitive (GSI) behaviour inferred to
87 result from dislocation glide and cross slip (Renner *et al.*, 2002; De Bresser, 2002). The
88 utilisation of flow laws for predicting rheological behaviour requires knowledge of flow-law
89 parameters, such as the stress exponent, n , the grain size exponent, p , and the activation energy,
90 Q . Most of the parameters are derived from laboratory experiments under well-constrained
91 conditions but inferring these parameters for the materials that constitute specific natural fault
92 zones can be challenging. Strain rates during experiments performed to constrain flow-law
93 parameters are orders of magnitude lower than those occurring during seismic slip on natural
94 faults and therefore predicting deformation mechanisms during seismic slip requires the flow
95 laws to be extrapolated in stress/strain rate. While it is difficult to test the accuracy of such

96 extrapolations based on mechanical data from high-velocity deformation experiments,
97 microstructural analyses offer critical additional datasets against which to test the accuracy of
98 flow-law predictions.

99 To constrain deformation mechanisms during seismic events, we characterise the micro-
100 and nanostructures of natural carbonate fault rocks directly at the slip interface using multiscale
101 crystallographic orientation analyses. The fault-rock microstructures reveal that crystal plasticity
102 contributed during deformation and that the microstructure was potentially modified by
103 annealing.

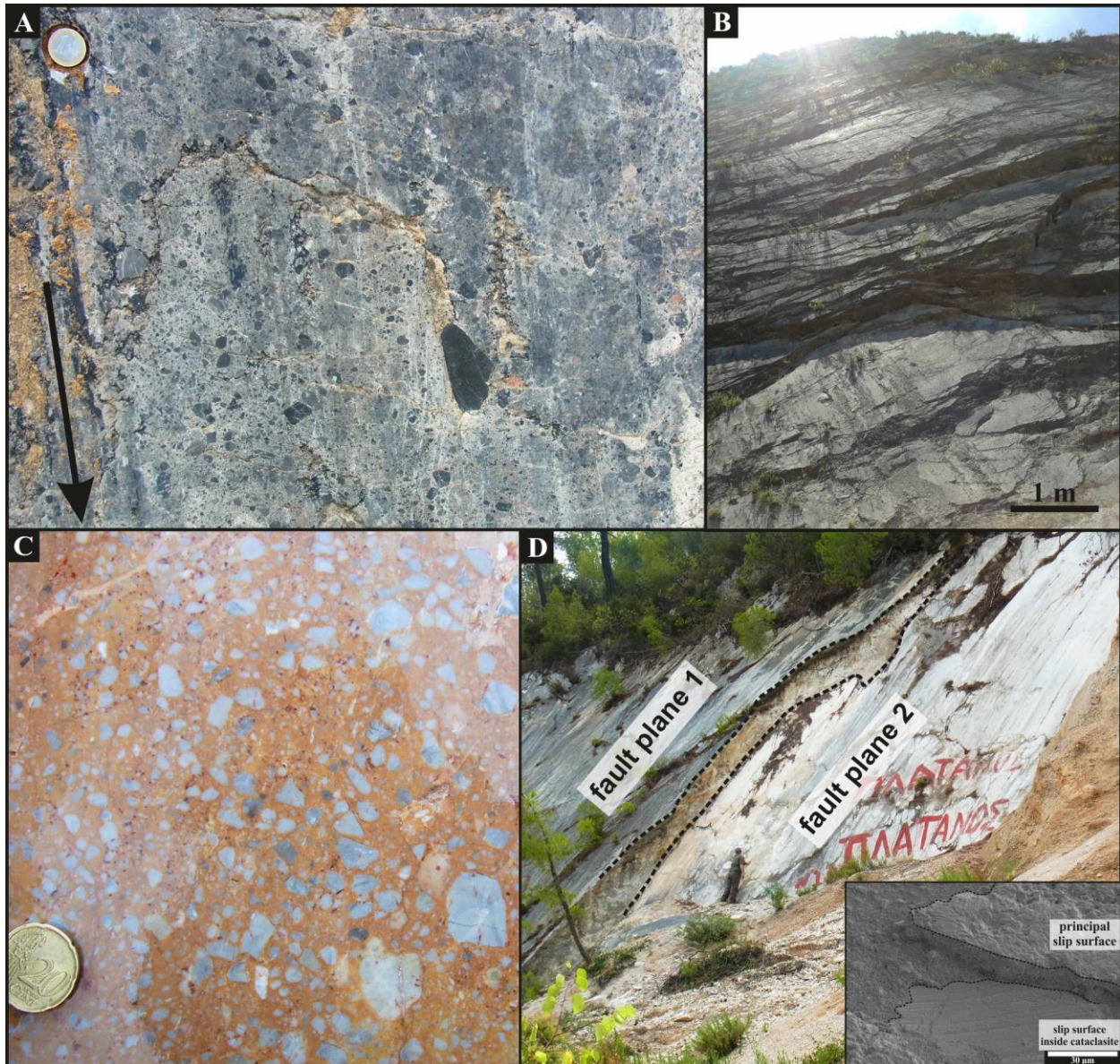
104 2 Geology and tectonic setting

105 The first investigated fault exposure (38°43'56.17"N, 23°0'27.41"E) is located close to
106 Arkitsa, along the northern coast of the Gulf of Evia, Greece. In general, the northward-dipping
107 fault planes (ESE-WNW strike) separate Triassic to Middle/Late Jurassic platform carbonates of
108 the footwall from lower Pliocene-Pleistocene up to Quaternary hanging-wall sediments
109 (Kokkalas *et al.*, 2007). The footwall cataclasite is a greyish, matrix-supported fault rock with
110 incorporated host-rock clasts (Fig. 1A). Multiple fault planes are hosted inside the damage zone,
111 indicating fault-plane overstepping (Fig. 1B). Records of historic seismicity document ~13
112 events since 426 BC with the last major nearby event in 1894 (M_s 6.9)(Ambraseys and Jackson,
113 1990).

114 The second fault exposure (38° 2'14.40"N, 23° 0'22.33"E) is located close to Schinos,
115 Corinth area. The fault plane dips towards the north, having an E-W strike. Upper Triassic
116 limestones and dolomites host the fault plane (Kaplanis *et al.*, 2013). The footwall fault rock is a
117 reddish cataclasite with light-grey host-rock clasts (Fig. 1C). In the field, the fault-plane
118 exposure shows at least one stepover (Fig. 1D). The last seismic event in the region was recorded

119 with three main shocks in February 1981 with a maximum magnitude of M_s 6.7 (Collier *et al.*,
120 1998).

121 Subduction-related back-arc volcanism, combined with extensional tectonics caused by
122 rollback of the Hellenic subduction zone (Thomson *et al.*, 1998), results in a high geothermal
123 gradient across the Aegean region (Papachristou *et al.*, 2014; Lambrakis *et al.*, 2014). The
124 geothermal gradient measured from geothermal exploration boreholes in the Sperchios basin,
125 approx. 50 km west of Arkitsa, is 35 °C/100 m (Metaxas *et al.*, 2010). Measurements at Kamena
126 Vourla indicate 46 °C at 200 m depth (Mendrinis *et al.*, 2010). Temperature constraints for the
127 Arkitsa fault, based on clay-mineral assemblages, indicate hydrothermal-fluid temperatures of
128 100–150 °C (Papoulis *et al.*, 2013). However, the clay layer is located inside the hanging-wall
129 breccia and may not be in direct relation to processes and temperatures on the fault plane. Also,
130 in the Sousaki-Loutraki region close to Schinos, geothermal exploration drilling revealed high
131 temperatures at shallow depth. In this region, (Mendrinis *et al.*, 2010) measured 63 °C at 500–
132 1100 m depth, which is in agreement with (Lambrakis *et al.*, 2014) obtaining ≥ 75 °C at 600–
133 900 m depth.



134
 135 *Figure 1: Overview of geological features. **A:** View onto Arkitsa fault plane. Dark, large host-rock clasts are*
 136 *incorporated into the light-grey footwall cataclasite. Arrow indicates slip direction. One-Euro coin for scale. **B:***
 137 *Multiple slip planes hosted inside the damage zone of the Arkitsa fault exposure exhibit overstepping. **C:** View onto*
 138 *Schinos fault plane. Light-grey host rock clasts incorporated into red hanging-wall cataclasite. **D:** Field view of*
 139 *Schinos fault plane exposure. Two distinct and overstepping fault planes are visible, hosted inside the damage zone.*
 140 *Person for scale. **Inset:** Secondary electron image showing development of secondary slip surface inside the Schinos*
 141 *footwall cataclasite. The secondary slip surface is situated about 10 μm below the principal slip surface.*

142

143

144

145 3 Methods

146 3.1 Crystal orientation acquisition

147 Thin sections were prepared from drill cores by cutting parallel to the slip direction and
148 normal to the slip surface. Electron backscatter diffraction (EBSD) data were acquired using a
149 Philips XL30 scanning electron microscope (SEM) equipped with an Oxford Instruments
150 Nordlys 2 CCD camera. Maps were acquired with an accelerating voltage of 30 kV, probe
151 current of 9.5 nA, and step size of 0.5 μm for the Arkitsa sample and 20 kV accelerating voltage,
152 9.5 nA probe current, 0.7 μm step size for the Schinos sample.

153 Crystal-orientation data were also acquired in a transmission electron microscope (TEM)
154 using the automatic crystal orientation mapping technique (ACOM-TEM, (Rauch and Véron,
155 2014)). TEM foils were prepared with a FEI Helios G3 focussed ion-beam scanning electron
156 microscope (FIB-SEM). ACOM-TEM data were acquired using the NanoMEGAS
157 ASTAR/SPINSTAR system on a FEI Tecnai G²-20 twin. Beam conditions during ACOM-TEM
158 were 200 kV and spot size 11, giving a nominal 1 nm probe diameter, resulting in a step size of 2
159 nm. During acquisition, the primary electron beam was set to precession movement, with an
160 opening angle of 0.5°. In a separate step, the acquired electron diffraction patterns are matched
161 with a pre-calculated bank file containing the simulated crystal orientations in kinematic
162 conditions, resulting in a unique crystal-orientation solution.

163 3.2 Data treatment

164 Orientation data from EBSD and ACOM-TEM were processed using the MTEX 4.5.2
165 toolbox (Hielscher and Schaeber, 2008; Bachmann *et al.*, 2011). The reference frame was set to
166 x-axis to the east, y-axis to the south and z-axis out of plane. Grain boundaries were defined as
167 misorientation angles $>10^\circ$ and subgrain boundaries were defined as misorientation angles in the

168 range 1–10° for EBSD and 2–10° for ACOM-TEM. Unindexed pixels or single pixels matched
169 as a different phase were removed and unindexed pixels were filled with the average orientation
170 of their grain neighbours. Grains <5 pixels were removed from EBSD datasets. Grains and
171 subgrains <20 pixels were removed from the ACOM-TEM dataset. A Kuwahara filter with a
172 kernel size of 5x5 was applied to the ACOM dataset to reduce orientation noise. All crystal
173 orientation plots were visualized before denoising to guard against the introduction of artefacts.
174 Contoured pole figures are based on one-point-per-grain orientation data. The optimum half-
175 width for contoured EBSD pole figures was estimated using the De la Vallée Poussin kernel
176 approach. Because of a low estimated optimum half-width for the ACOM-TEM data, we chose
177 15° to match the EBSD pole figures. Misorientation inverse pole figures (MIPF) were plotted for
178 subgrain-boundary misorientation angles of 1–10° for EBSD and 2–10° for ACOM-TEM.

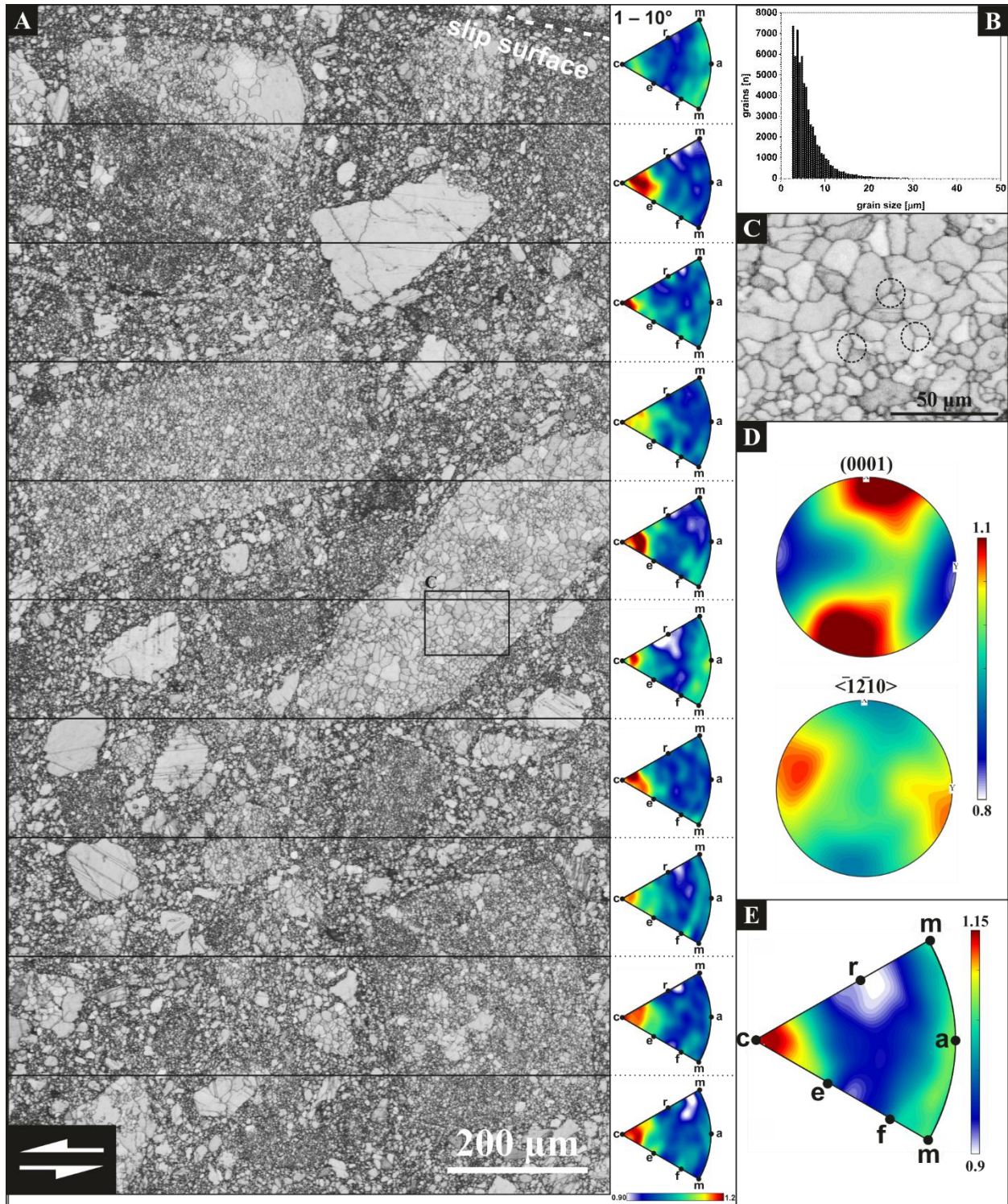
179 **3.3 Grain size analysis**

180 A grain-size distribution was determined from the EBSD and ACOM-TEM data. The ACOM-
181 TEM grain-size distribution was based on a grain-boundary trace map by combining a reliability
182 map and an indexed crystal-orientation map. For the fractal dimension analysis, the calculated
183 grain-size frequencies from the ACOM-TEM data were scaled with the difference in area
184 resolution, due to differences in step size, by a factor of 62500. A 500x500 nm pixel (EBSD) was
185 divided by a 2x2 nm pixel (ACOM-TEM) leading to 62500. To obtain a grain-size distribution,
186 we chose the dataset binning to be continuous (i.e., equal to the mapping step size), to reduce
187 undersampling of small grains. Each dataset was individually fitted with a linear equation where
188 the slope of the linear fit in log-log space equals the fractal dimension D . The grain-size bin
189 width for the fractal-dimension plot was set to 1 μm to account for the large number of small
190 grains.

191 4 Results

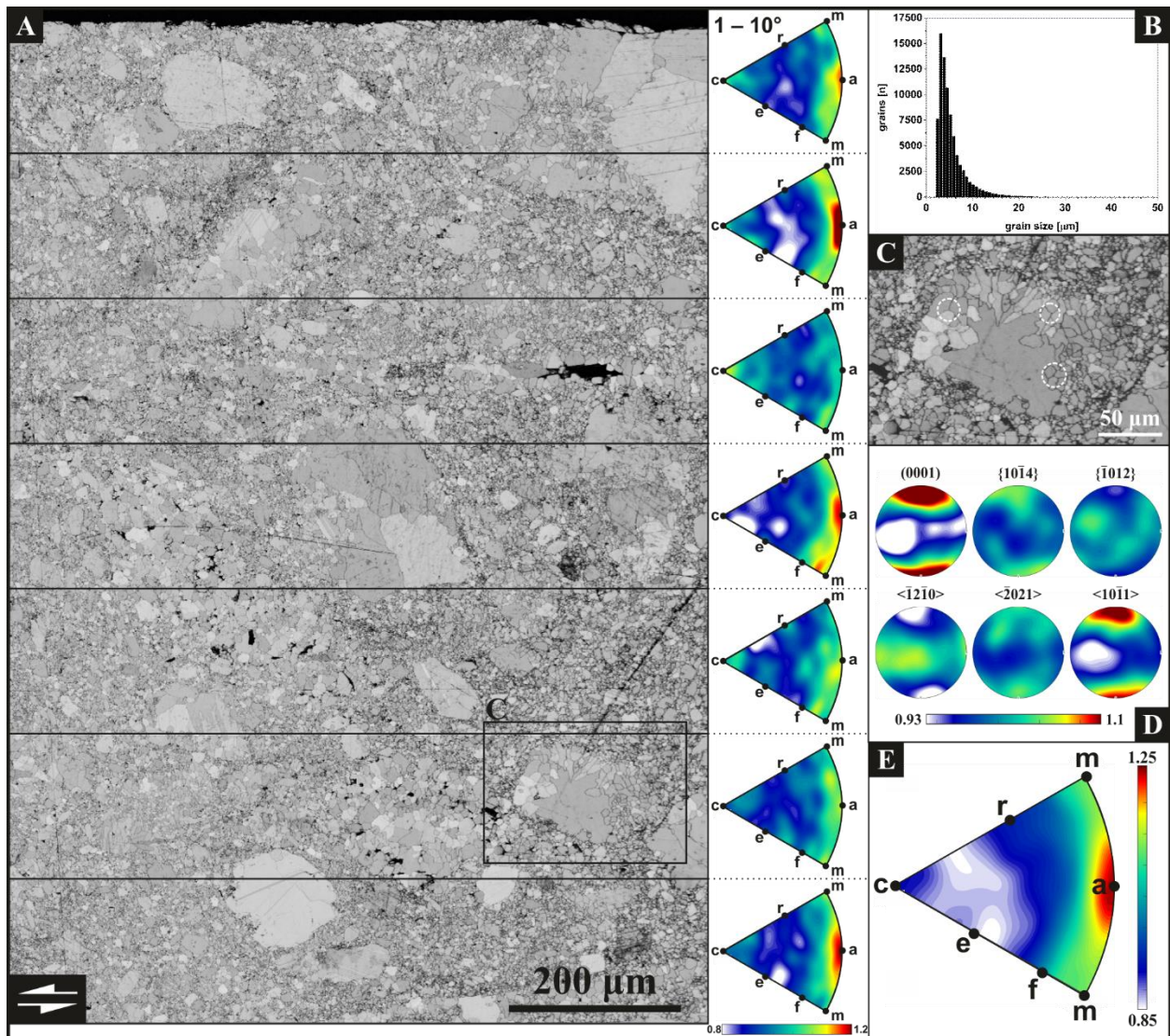
192 4.1 Microscale crystal-orientation data

193 Figure 2A presents the EBSD map of the Arkitsa footwall cataclasite. The map exhibits
194 small matrix-forming grains and larger host-rock clasts, where the clasts show an internal fine-
195 grained foam microstructure. The fine-grained matrix and the foam microstructure display
196 straight grain boundaries that meet in 120° triple junctions (Fig. 2C and A). Grain boundaries are
197 typically not aligned over distances greater than one grain diameter. Monocrystalline calcite
198 clasts occasionally host twin lamellae. An elongated host-rock grain at the top left of Figure 3A
199 exhibits a transitional state between monocrystalline and polycrystalline calcite. The median
200 grain size is $5.0\ \mu\text{m}$ (Fig. 2B). MIPFs for each subset in Figure 2A reveal concentrations of
201 misorientation axes approximately centred on $[0001]$. The pole figures of (0001) and $\langle\bar{1}2\bar{1}0\rangle$
202 (Fig. 2D) display a weak CPO with multiples of uniform distribution (MUD) in the range 0.8–
203 1.2. The (0001) planes are parallel to the slip plane and the $\langle\bar{1}2\bar{1}0\rangle$ axes are parallel to the slip
204 direction (noting the orientation of the trace of the slip surface at the top right of Fig. 2A). The
205 subgrain-boundary MIPF for the overall map data exhibits a cluster of misorientation axes
206 parallel to $[0001]$ (Fig. 2E), like the individual subsets in Fig 2A.



207
 208 *Figure 2: Electron-backscatter diffraction results of the Arkitsa fault exposure. **A:** Band-contrast map and MIPF for*
 209 *each subsection. Fault surface with hanging-wall in top-right corner. **B:** Grain-size distribution **C:** Detailed view of*
 210 *host-rock clast microstructure. Black circles mark triple junctions and 120° angles. **D:** Pole plots of (0001) planes*
 211 *and $\langle 12\bar{1}0 \rangle$ axes in the same reference frame as the map in A. **E:** MIPF of the full map area. Labels indicate*
 212 *crystal directions or plane normals. Contours are multiples of uniform distribution.*

213 Figure 3A presents the EBSD results from the Schinos footwall cataclasite. The band-
214 contrast map reveals a microstructure with large calcite host-rock grains incorporated into the
215 cataclasite matrix. Like Figure 2A, several host-rock grains are in a transitional state from
216 monocrystalline to polycrystalline (Fig. 3C). Whilst many grain boundaries are curved, several in
217 both the matrix and host-rock grains are straight and meet in 120° triple junctions (Figure 3C,
218 white circles). The outer margins of the host-rock grains display a rim with grain boundaries,
219 creating an incipient core-mantle structure (Fig. 3C). The median grain-size is $4.4 \mu\text{m}$. (Fig. 3B).
220 The pole figures in Figure 3D display a weak CPO with multiples of uniform distribution (MUD)
221 in the range 0.8–1.2. The (0001) planes are parallel to the slip plane and the $\langle\bar{1}2\bar{1}0\rangle$ axes are
222 parallel to the slip direction. Furthermore, $\{10\bar{1}4\}$ poles exhibit a weak cluster approximately
223 parallel to the slip-plane normal and the $\langle\bar{2}021\rangle$ axes exhibit three maxima sub-perpendicular to
224 the slip plane. In addition, $\{\bar{1}012\}$ planes exhibit one maximum and a girdle, whereas $\langle 10\bar{1}1\rangle$
225 directions are oriented perpendicular to the slip plane. MIPFs for subgrain-boundary
226 misorientation axes in each vertical section in Figure 3A exhibit a pronounced maximum centred
227 on the $\langle a\rangle$ direction. Secondary maxima are centred on $\langle m\rangle$, $\langle c\rangle$, or $\langle a\rangle$, or a combination of
228 all three directions. The overall MIPF in Figure 3E exhibits subgrain misorientation axes
229 predominantly around $\langle a\rangle$, consistent with most misorientation axes in the vertical sections from
230 Figure 3A.



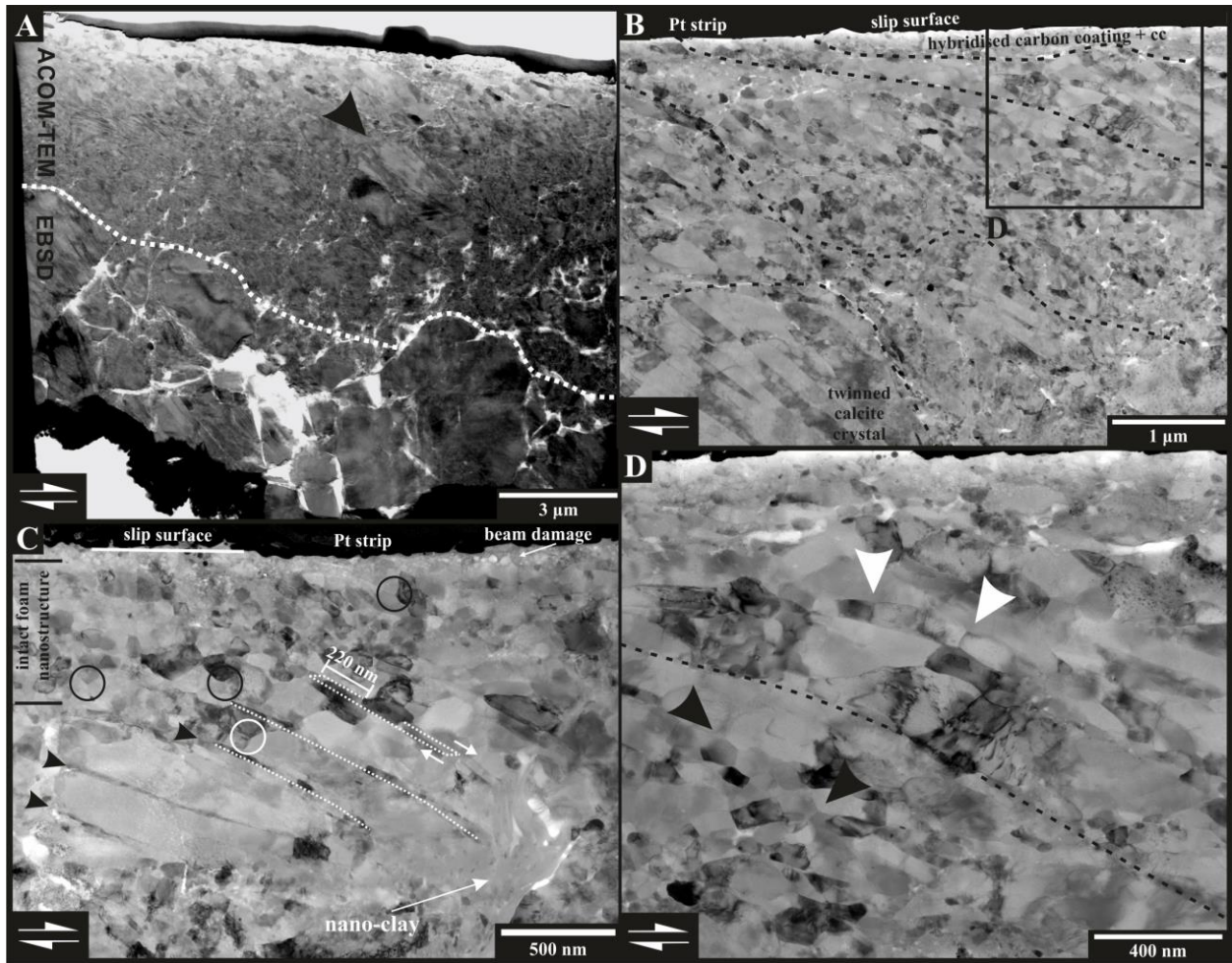
231
 232 *Figure 3: Electron-backscatter diffraction results of the Schinos fault exposure. **A:** Band-contrast map and MIPF*
 233 *for each subsection. Fault surface at the top (black). **B:** Grain-size distribution. **C:** Clast in matrix displaying a*
 234 *mantle of grains around a host-rock clast with internal triple junctions (white dashed circle). **D:** Combined pole*
 235 *plots of relevant slip systems from A. **E:** Misorientation inverse pole figure from the full dataset in A.*

236 4.2 Nanostructures

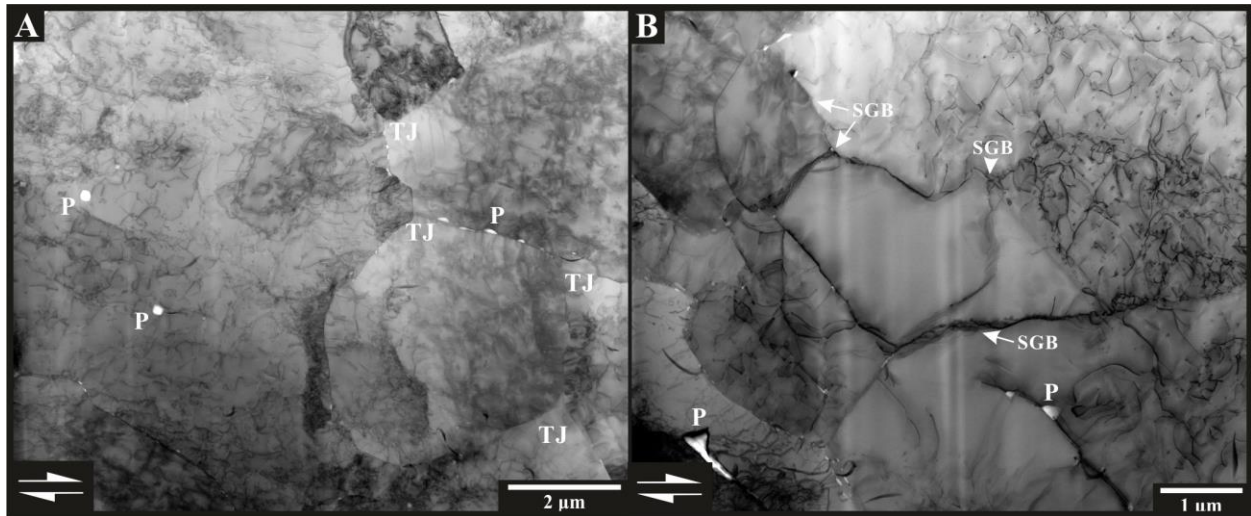
237 TEM investigation of the Arkitsa fault rock reveals a fine-grained volume situated on
 238 coarser grains (Fig. 4A). The first 15–20 μm of material directly below the PSS exhibits a foam
 239 nanostructure. This foam nanostructure consists of grains with approximately equal grain size
 240 and straight grain boundaries that meet in triple junctions with 120° angles (Fig. 4C). The grains
 241 in this zone are often sandwiched between, and overprinted by, linear discontinuities (e.g., Fig.

242 4C, white lines) dipping at an angle of about 30° to the slip surface into the nanogranular
243 material. The linear discontinuities can displace single grains (Fig. 4B and C) or form bands of
244 localised deformation with a sigmoidal appearance, preserving the intact foam nanostructure in
245 between (Fig 4B and D). In Figure 4C, grains with similar contrast are displaced about 220 nm
246 along these planes. These discontinuous planes cannot be traced to the slip surface (Fig. 4C) but
247 terminate in an area with a smaller grain size below the PSS (Fig. 4C). Larger grains are
248 occasionally intermingled in the nanogranular material (Fig. 4A). Below the nanogranular
249 material, twinned calcite grains of 3–5 µm in diameter mark the beginning of the cataclasite (Fig.
250 4A). The grain size at the transition between the slip-surface nanostructure and the larger grains
251 corresponds to the grain sizes observed in the EBSD map (Fig. 4A and D).

252 Figure 5A and B present the nanostructure of the Schinos fault directly at the PSS.
253 Compared to the Arkitsa sample (Figure 4A and C), the grain size is larger, resulting in a less
254 complex nanostructure. The Schinos nanostructure exhibits straight grain-boundary morphology
255 with triple junctions (Fig. 5A) and subgrain boundaries (Fig. 5B). The average dislocation
256 density in the larger Schinos grains is $\sim 1.5 \times 10^{13} \text{ m}^{-2}$. The dislocation density decreases towards
257 the subgrain boundaries but otherwise the distribution is generally homogeneous except for some
258 subgrain interiors that are devoid of dislocations (Fig. 5B).



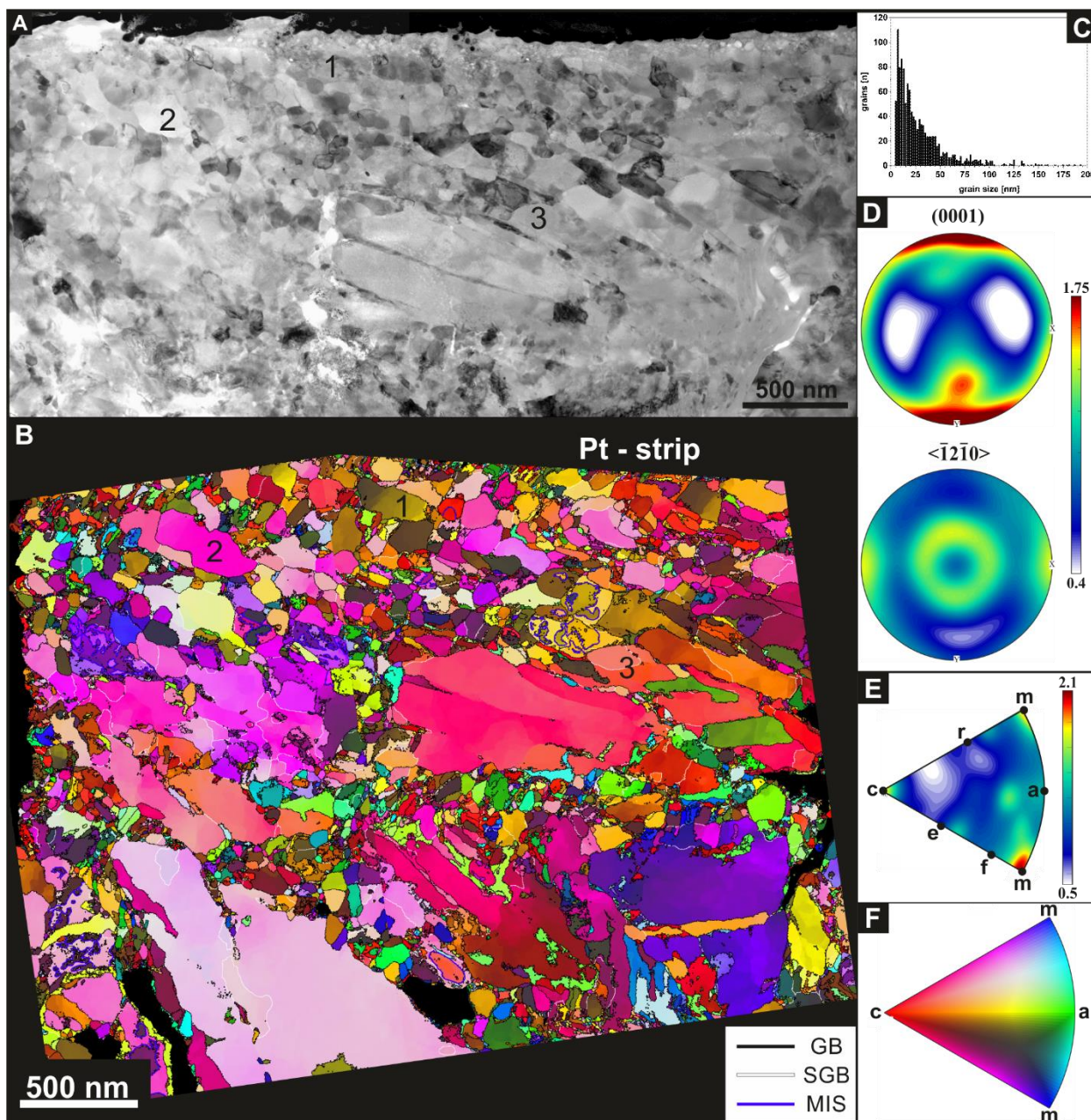
259
 260 *Figure 4: Arkitsa fault exposure nanostructures. **A:** Bright-field (BF) TEM overview of deformed volume with a*
 261 *sharp boundary to the footwall cataclasite (dashed line). The grain size of the less deformed grains is about 3–5 μm .*
 262 ***B:** Bright-field STEM image with detailed view of the deformed volume. Anastomosing boundaries separate*
 263 *alternating domains of deformed and intact foam nanostructure (dashed lines). **C:** Bright-field STEM image*
 264 *showing intact foam nanostructure with triple junctions and 120° angles adjacent to the slip surface (black circles).*
 265 *Fractures that dissect grains lose trace inside intact foam nanostructure. Older foam nanostructure is preserved*
 266 *between fracture planes (white circle). **D:** Bright-field STEM image of detailed view from **B**. Deformed foam*
 267 *nanostructure with former triple junctions while having a sheet-like structure (white arrows) next to intact foam*
 268 *nanostructure (black arrows).*



269
 270 *Figure 5: Schinos fault exposure nanostructures. **A:** BF-STEM image with overview of dislocation structure*
 271 *showing triple junctions (TJ) and grains with dislocation densities of $1.5 \times 10^{13} \text{ m}^{-2}$ and higher. **B:** BF-STEM image*
 272 *with dislocation-free subgrain in the centre surrounded by subgrain boundaries (SGB). Dislocation density of*
 273 *surrounding grain interiors decreases towards the SGBs. P = pores.*
 274

275 4.3 Nanoscale crystal-orientation (ACOM-TEM) data

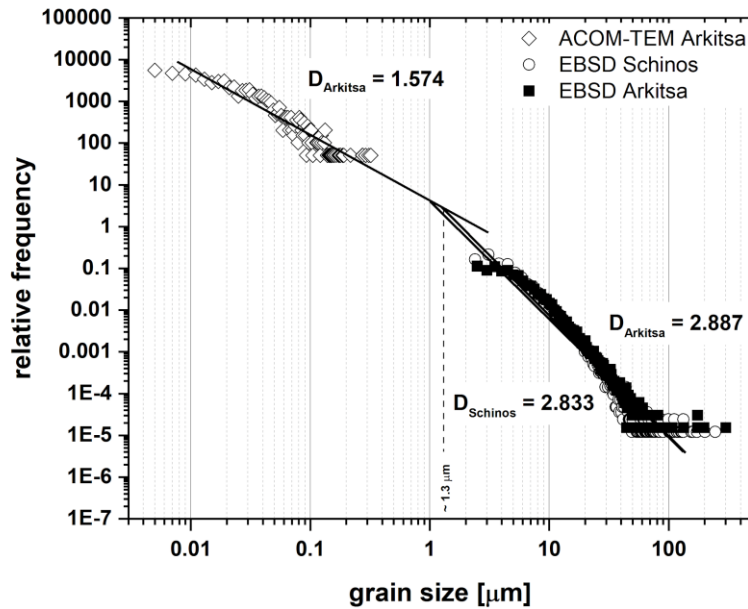
276 Figure 6 presents the ACOM-TEM data acquired on a subset of the same FIB foil shown
 277 in Figure 4C, reproducing the bright field (BF-)TEM nanostructure (Fig. 4C, 6A and B). Pole
 278 figures constructed from the crystal-orientation map exhibit a CPO with (0001) densities in the
 279 range 0.4–2.0 MUD in the highly deformed, fine-grained region below the PSS. Some grains
 280 exhibit an orientation spread indicating intragranular misorientation (Fig. 6B). The median grain-
 281 size is 21 nm (Fig. 6C), albeit ranging between 5 to 300 nm. Contoured pole figures (Fig. 6C)
 282 reveal a CPO with [0001] axes oriented perpendicular to the slip surface and $\langle \bar{1}2\bar{1}0 \rangle$ axes
 283 clustered sub-parallel to slip direction. A second clustering of $\langle \bar{1}2\bar{1}0 \rangle$ axes appear as a ring
 284 around the centre of the pole figure. The MIPF of the subgrain misorientation axes exhibits
 285 maxima parallel to [c] and $\langle m \rangle$.



286
 287
 288 **A:** BF-STEM image from Figure 4C. **B:** Crystal-orientation map colour-coded according to the inverse pole figure
 289 in **F** indicating the crystal direction aligned with the Y-axis of the map. **C:** Grain-size distribution of map in **B**. **D:**
 290 Contoured pole figures of (0001) poles and $\langle \bar{1}2\bar{1}0 \rangle$ axes. **E:** MIPF of misorientation axes associated with
 291 misorientation angles in the range 2–10°. **F:** IPF-Y colour key for map in **B**. GB = Grain boundary, SGB =
 292 Subgrain boundary, MIS = Misindexed grain boundary. Due to the electron-transparent nature of the FIB foil and
 293 corresponding diffraction behaviour, grain boundary morphologies are less well pronounced in the ACOM-TEM
 294 data compared to the BF-STEM image.

295 **4.4 Grain-size distribution**

296 Figure 7 presents a log-log plot of relative frequency as a function of grain size from the EBSD
297 and ACOM-TEM data. A data gap between 350 nm and 2 μm arises from the different spatial
298 resolutions and area coverage of the two techniques. The EBSD-based fractal dimension of the
299 Arkitsa fault exposure is $D = 2.887$ ($R^2 = 0.912$), while the fractal dimension of the ACOM-TEM
300 data is $D = 1.574$ ($R^2 = 0.895$). The EBSD-based fractal dimension of the Schinos sample is $D =$
301 2.833 ($R^2 = 0.902$). Extrapolations of the two different types of data set intersect at a grain size
302 of approximately 1 μm .



303
304
305 *Figure 7: Fractal dimension plot of grain-size data from both fault exposures. The fractal dimensions of the Arkitsa*
306 *datasets are $D = 2.887$ (EBSD) and $D = 1.574$ (ACOM-TEM). The fractal dimension of the Schinos dataset is $D =$*
307 *2.833 (EBSD).*
308

309
310
311
312

313 5 Discussion

314 5.1 Grain fragmentation and fractal dimensions

315 Brecciation and cataclasis are important mechanisms of grain-size reduction in fault
316 zones. Whereas intragranular extensional fracturing governs cataclasis during early fault-slip
317 through particle-particle fragmentation, chipping governs the late stages during which grain
318 edges are removed after greater amounts of fault displacement (Ferraro *et al.*, 2018). Cataclasis
319 can produce different grain-size distributions with fractal dimensions (D) that provide
320 information on the characteristics of fracturing (Sammis *et al.*, 1986; Sammis *et al.*, 1987;
321 Blenkinsop, 1991). For example, a fractal dimension of $D = 2.580$ can result from the self-
322 similar fracturing of a three-dimensional object, such as a cube. In addition to obtaining D via
323 linear fitting, one can also determine D via:

$$324 \quad D = \frac{3 \log(f)}{\log(F)} + 3 \quad (1)$$

325 where F is the number of fragments created, and f is the fragmentation fraction, defined as $f =$
326 C/F , with C being the number of fragments that are fragmented further (Heilbronner and Barrett,
327 2014). For a three-dimensional object with $F = 8$ it follows that for $f = 8/8$, 100 % of the newly
328 formed grains are fragmented again, which results in a fractal dimension of $D = 3.000$. Our
329 fractal dimensions of $D = 2.887$ and $D = 2.833$ (Fig. 7) can be achieved with a fragmentation
330 fraction of $f = 7/8$, giving $D = 2.807$. The agreement between the theoretical and our measured
331 values suggests that the cataclasite experienced a high degree of fragmentation due to particle-
332 particle interaction. Furthermore, a value of $D = 1.574$ from ACOM-TEM (Fig. 7) may
333 correspond to a low degree of fragmentation with $f = 3/8$ yielding $D = 1.585$ (see eq. 1). We
334 propose that the difference in D between the bulk cataclasite and the nanogranular volume arises
335 from a difference in the degree of fragmentation. A lower D of 1.574 may, therefore, indicate a

336 different control on particle size involving a minor degree of particle-particle fragmentation. We
337 suggest that the change in fractal dimension within the same fault rock may reflect a change in
338 fragmentation and thus deformation mechanisms, as also proposed by (Keulen *et al.*, 2007).

339 **5.2 Nanostructures**

340 The Arkitsa and Schinos faults exhibit different nanostructures in their principle slip zones
341 (PSZs). Whereas the PSZ of the Arkitsa fault is complex directly below the slip surface and
342 includes a layer of nanograins (Figs. 4 and 6), the PSZ of the Schinos fault exhibits a similar
343 grain size as its bulk fault rock (Figs. 3 and 5). The difference in nanostructural complexity
344 suggests that the Schinos fault represents an earlier stage of fault-rock evolution compared to the
345 Arkitsa fault, whereas the nanostructure of the Arkitsa fault suggests multiple slip events and a
346 more extended deformation history.

347 Slip along the PSS would result in the introduction of plastic strain accompanied by a
348 thermal spike through shear heating (Rice 2006) during a seismic event. The Schinos
349 nanostructure, with a high, free dislocation density and triple junctions (Fig. 5A and B),
350 resembles the structural appearance of metals subjected to a process known as cold-rolling and
351 annealing (Humphreys and Hatherly, 2004). The procedure involves the introduction of high
352 plastic strain followed by static high-temperature treatment to induce microstructural changes.
353 The typical range for industrial cold-rolling is about 60–180 °C (Hollandt *et al.*, 2010),
354 corresponding to 0.05–0.11 of the melting temperature, T_m , for steel. It is likely that the
355 temperature during the onset of slip of the carbonate faults corresponds to a homologous
356 temperature of about 0.2 T_m (300 °C). Cold-rolling and subsequent annealing is a well-
357 established process in engineering (Humphreys and Hatherly, 2004) leading to grain-boundary
358 migration and recrystallisation. Dislocation introduction through strain pulses in the low-

359 temperature plasticity regime can result in strain-hardening effects. The yield strength increases
360 through dislocation entanglement and dislocation back-stresses, which are reduced during
361 annealing. Addition of thermal energy through heating enables dislocation climb and solid-state
362 diffusion, leading to recovery or recrystallisation by static grain growth or grain boundary
363 migration. The resulting grain size is smaller compared to the previous microstructure leading to
364 grain-boundary strengthening and hence, toughening of the material. Such deformation processes
365 followed by annealing of the material are already documented in experimentally and naturally
366 deformed olivine (Druiventak *et al.*, 2012; Matysiak and Trepmann, 2012) and quartz (Trepmann
367 and Stöckhert, 2013; Trepmann *et al.*, 2017). Repeated straining and subsequent annealing can
368 lead to grain-size reduction and may, therefore, pose an additional mechanism of nanograin
369 formation.

370 The 120° triple junctions of the Arkitsa nanostructure may indicate annealing by grain
371 boundary migration (Figs. 2 and 4). Static recrystallization involves an initial stage during which
372 deformed grains with high, stored strain energy are replaced by recrystallized grains, which may
373 then continue to grow. To evaluate whether significant grain growth can occur during the
374 postseismic and inter-seismic period, we use the following kinetic model (Covey-Crump, 1997),

$$375 \quad d^{1/n} - d_0^{1/n} = k t = k_0 t \exp(-H/RT) \quad (2)$$

376 where d is the final grain size, d_0 the initial grain size, n is a dimensionless constant, k_0 is a pre-
377 exponential factor, t the duration of grain growth and H is the apparent activation enthalpy. The
378 values of n and H depend on the growth-controlling process. In the case of a grain-boundary
379 controlled system, with no second phases (pure system) $n = 0.5$. For an impure system where
380 coalescence of a second phase occurs by volume diffusion (wet case) $n = 0.33$ and for an impure
381 system where coalescence of a second phase occurs by grain-boundary diffusion, $n = 0.25$

382 (Covey-Crump, 1997). Assuming fluid-present conditions based on observations that suggest the
383 presence of portlandite ($\text{Ca}(\text{OH})_2$) during deformation (Ohl et al. 2020), we set $n = 0.33$. This
384 interpretation results in the following parameters: $1/n \approx 3$, $k_0 = 2.514 \times 10^9 \mu\text{m}^n \text{s}^{-1}$ and $H =$
385 $173.6 \text{ kJ mol}^{-1}$ (Covey-Crump, 1997). To assess the potential for fluid-assisted post-seismic grain
386 growth due to the ambient temperature at depth, we consider the borehole temperatures from the
387 outcrop areas (Metaxas *et al.*, 2010; Papoulis *et al.*, 2013; Lambrakis *et al.*, 2014). We assume a
388 geothermal gradient of 65–75 °C/km and a typical seismogenic crustal depth of 3–5 km (Scholz,
389 1988) resulting in an ambient temperature of about 300 °C. Annealing of the nanostructure for
390 one year, at a temperature of 300 °C, with $d_0 = 0.1 \mu\text{m}$, leads to a final grain size of $d = 2.3 \mu\text{m}$.
391 Therefore, not only under short-lived, co-seismic temperature spikes but also during the inter-
392 seismic period, grain growth may contribute to the formation and modification of the
393 microstructure. However, the grain-size distribution in Figure 6B contains grains $< 50 \text{ nm}$ in
394 size, illustrating that our grain-growth approximation provides an upper limit. Nonetheless, our
395 assessment of inter-seismic grain growth supports our suggestion that high-plastic strain
396 deformation and short annealing times are an alternative mechanism to form a cohesive
397 nanogranular fault rock.

398

399 **5.3 Deformation mechanisms**

400 **5.3.1 Grain-boundary sliding**

401 GBS has been proposed as a deformation mechanism for fine-grained fault rocks during
402 seismic slip (De Paola *et al.*, 2015). Langdon (2006) describes two possible types of GBS:
403 Rachinger sliding and Lifshitz sliding. Rachinger sliding is defined by the relative displacement
404 of adjacent grains, with strain compatibility maintained by dislocation motion in grain interiors.

405 Therefore, Rachinger sliding is often referred to as dislocation-accommodated grain-boundary
406 sliding in the geological literature (Hirth and Kohlstedt, 1995; Hansen *et al.*, 2011). In contrast,
407 Lifshitz sliding is coupled to vacancy diffusion along stress gradients during Nabarro-Herring or
408 Coble diffusion creep. GBS is an essential process that contributes to superplasticity, which is
409 the ability of a material to deform to strains on the order of 1000% without failure (Langdon,
410 2006; (Komura *et al.*, 2001). Therefore, the term superplasticity does not indicate a deformation
411 mechanism but is a phenomenological description. In experiments on metals (Langdon, 2006)
412 and calcite (Schmid *et al.*, 1977; Rutter *et al.*, 1994) superplastic behaviour is most pronounced
413 in a regime in which strain rate is proportional to approximately the square of both stress and
414 grain size. This mechanical behaviour is associated with Rachinger sliding in materials with
415 grains that are generally too small to host subgrain boundaries (Langdon, 2006). An important
416 consideration for seismogenic faults is that experiments by (Komura *et al.*, 2001) on metals
417 demonstrate a strong strain-rate dependence for superplasticity, where strain rates $> 1 \text{ s}^{-1}$ reduce
418 the achievable strain from 1000 % down to 100 %. This observation presents a challenge to the
419 interpretation of superplastic behaviour from micro-, or nanostructures in the high-strain rate
420 context of co-seismically produced materials.

421 In many metals, GBS is proposed as a deformation mechanism of nanogranular materials.
422 The *in-situ* TEM deformation study by (Kumar *et al.*, 2003) on nanograined Ni with grain sizes
423 $< 30 \text{ nm}$ revealed that GBS can be an important deformation mechanism even at room
424 temperature. Those authors report the involvement of dislocations during the deformation
425 process and emphasize the dominant role of dislocation-mediated plasticity. Experimental
426 evidence suggests that at grain sizes of $< 20 \text{ nm}$ the material strength decreases and produces an
427 inverse Hall-Petch effect (Kumar *et al.*, 2003). Another study by Lu *et al.* (2000) also indicates

428 that GBS may be significant in nanomaterials at lower homologous temperatures. At grain sizes
429 below 10 nm dislocation activity ceases and GBS dominates. Whether *in situ* nanoscale
430 deformation behaviour within a TEM can be generalised to be representative of bulk deformation
431 behaviour remains a matter of debate (Ma, 2004). Nevertheless, deformation of materials with
432 grain sizes ≥ 30 nm that involves GBS can also involve dislocation activity. The combination of
433 dislocations we observe (Figs. 4 & 5), subgrain boundaries in EBSD (Figs. 2 & 3), and the
434 nanoscale CPO consistent with the activity of known slip systems (Figure 6) suggests that
435 dislocation activity plays an important role during the formation and deformation of the
436 nanostructure.

437 A mechanism that combines GBS and dislocation activity is disGBS. This mechanism
438 has been proposed as a deformation mechanism for several minerals, including calcite (Walker *et al.*,
439 1990), olivine (Hirth and Kohlstedt, 1995; Hansen *et al.*, 2011), and quartz (Tokle *et al.*,
440 2019). Based on the microstructures and mechanical data from their experiments on olivine,
441 Hansen *et al.* (2011) propose a similar disGBS mechanism to the model by Langdon (2006), in
442 which the subgrain size is smaller than the grain size. Dislocation activity during disGBS may be
443 an explanation for the CPO observed by Hansen *et al.* (2011) and may be an alternative
444 interpretation to crystal plasticity for the micro- and nanostructure observed here. Schmid *et al.*
445 (1977) and Walker *et al.* (1990) observed displacements across grain boundaries on the pre-cut
446 surfaces of deformed split cylinders deformed in regimes with non-linear stress dependencies.
447 Rutter *et al.* (1994) use the similarities of stress and grain-size exponents which fit with the later
448 proposed model by Langdon (2006). Likewise, several studies (e.g., Schmid *et al.*, 1977; Walker
449 *et al.*, 1990; Rutter *et al.*, 1994) have measured regimes in which the stress and grain-size
450 exponents of calcite are broadly in agreement with the models of disGBS reviewed by Langdon

451 (2006). Rutter *et al.*, (1994) report a CPO during high-temperature creep deformation, where one
452 of the experiments reached a strain of 600–1000 %, representing superplastic flow. Those
453 authors interpreted their results to indicate a contribution from intracrystalline plastic flow
454 involving cyclic dynamic recrystallisation but did not exclude the contribution of GBS.

455 High-strain torsion experiments ($\gamma = 20$) by Barnhoorn *et al.* (2005), however,
456 demonstrate that post-deformational annealing can change the microstructural appearance and
457 produce a foam structure where the grain morphologies are indistinguishable from a GBS
458 microstructure. The CPO formed during initial deformation is enhanced with progressive
459 annealing as the axis distributions become tighter. In addition, the degree of microstructural
460 evolution in calcite deformed by Barnhoorn *et al.* (2005) appears to be incomplete in comparison
461 to the starting material used and shares similarities with our microstructure (Fig. 2). These
462 similarities and a pronounced CPO across different scales suggest that the microstructures of the
463 studied carbonate faults may be influenced by other deformation processes than exclusively
464 GBS.

465

466 **5.3.2 Crystal-plasticity**

467 The occurrence of CPOs suggests the activation of one or more slip systems in both
468 Greek faults. Multi-scale analysis of crystal orientations (Figs. 2, 3 and 6) reveals that the CPO
469 present at the nanoscale in the PSZ is also present in the adjacent cataclasite. The distributions of
470 (0001) planes and $\langle \bar{1}2\bar{1}0 \rangle$ axes from the Arkitsa fault are consistent with CPOs present in
471 previous carbonates experimentally deformed under both seismic and sub-seismic conditions
472 (Smith *et al.*, 2013; Verberne *et al.*, 2013; Kim *et al.*, 2018; Demurtas *et al.*, 2019; Pozzi *et al.*,
473 2019). However, the experimental studies have not yet provided detailed slip-system analyses.

474 The combined evidence of calcite (0001) planes aligned parallel to the slip plane, $\langle\bar{1}2\bar{1}0\rangle$ axes
475 aligned parallel to the slip direction and the distribution of subgrain-misorientation rotation axes
476 indicates the activation of the (0001) $\langle\bar{1}2\bar{1}0\rangle$ glide system (Figure 2D and E). Subgrain-
477 boundary misorientation axes (Figure 2E) parallel [0001] are consistent with the presence of
478 twist boundaries parallel to the (0001) plane and consisting of $\langle\bar{1}2\bar{1}0\rangle$ screw dislocations whilst
479 misorientation axes around $\langle 10\bar{1}0\rangle$ are consistent with the presence of tilt boundaries consisting
480 of (0001) $\langle\bar{1}2\bar{1}0\rangle$ edge dislocations. Both types of boundaries can be produced by activation of
481 the (0001) $\langle\bar{1}2\bar{1}0\rangle$ glide system. We note that the ring pattern in the centre of the $\langle\bar{1}2\bar{1}0\rangle$ pole
482 figure (Figure 6C) is likely an artefact arising from diffraction pattern indexing during ACOM-
483 TEM analysis. De Bresser and Spiers (1997) performed a detailed experimental study on calcite
484 single crystals, in which they identified slip systems based on analysis of the traces of slip bands.
485 In their experiments, the (0001) $\langle\bar{1}2\bar{1}0\rangle$ slip system was activated in the temperature range of
486 600–800 °C.

487 In contrast to the Arkitsa fault, misorientation axes of subgrain boundaries in the Schinos
488 fault are dominantly parallel to $\langle\bar{1}2\bar{1}0\rangle$, with only secondary maxima parallel to $\langle 10\bar{1}0\rangle$ and
489 [0001] (Fig. 3). Misorientation axes parallel to $\langle\bar{1}2\bar{1}0\rangle$ indicate the presence of subgrain
490 boundaries consisting of edge dislocations on the $f\{\bar{1}012\}\langle 10\bar{1}1\rangle$ or $r\{10\bar{1}4\}\langle\bar{2}021\rangle$ slip
491 systems. In the experiments of (De Bresser and Spiers, 1997) the $f\{\bar{1}012\}\langle 10\bar{1}1\rangle$ slip system
492 was activated at temperatures between 600–800 °C, while $\{r\}$ slip was activated over a broader
493 temperature range of 300–800 °C. These two slip systems also exhibit different critical resolved
494 shear stress (CRSS). At temperatures > 600 °C, the CRSS for $f\langle 10\bar{1}1\rangle$ is less < 20 MPa and for
495 $r\langle\bar{2}021\rangle$ is ≤ 10 MPa. Overall, we suggest that the misorientation axes around $\langle\bar{1}2\bar{1}0\rangle$ (Figure
496 3A and E) most likely originate from edge dislocations on the $r\langle\bar{2}021\rangle$ slip system as the CPO

497 indicates that this system is more favourably aligned for slip than is the $f <10\bar{1}1>$ system. The
498 change from rotation around $\langle a \rangle$ to additional rotation around $[0001]$ and $\langle m \rangle$ indicates the
499 activation of more than one slip system, in particular the additional activation of $(0001)\langle \bar{1}2\bar{1}0 \rangle$.
500 The high temperatures indicated by the misorientation analyses are in agreement with our
501 previous estimates for these faults of 600–800 °C, but < 1000 °C, based on the degree of sp^2
502 hybridisation of partly-hybridised amorphous carbon (Ohl *et al.*, 2020). Whether the potential
503 high-temperature signals are diagnostic for deformation at co-seismic velocities warrants further
504 investigation. Because a systematic experimental study of slip systems in sub-seismic and
505 seismically deformed carbonate fault rocks is lacking, more experiments are required to
506 investigate potential differences in CPOs, including between dry and wet environmental
507 conditions.

508 To evaluate whether changes in slip systems indicate shear-heating induced temperature
509 gradients, we analysed EBSD subsets over a range of distances from the PSS to test for
510 systematic variation in the temperatures associated with the recorded slip systems (De Bresser
511 and Spiers, 1997). Overall, the Arkitsa (Fig. 2A) and Schinos (Fig. 3A) fault rocks do not exhibit
512 systematic changes in misorientation axes and hence slip systems or associated temperatures. If
513 the faults experienced seismic slip, a temperature gradient was not recorded. However, the
514 Schinos fault does display a non-systematic variation in the intensities of misorientation-axes
515 maxima parallel to $\langle \bar{1}2\bar{1}0 \rangle$ and $[0001]$, suggesting variation in the contributions of r -slip and
516 $(c)\langle a \rangle$. The underlying cause for the non-systematic changes in misorientation axes remains
517 unknown and warrants further investigation. Nevertheless, if we can reliably apply the slip
518 system-temperature correlations from De Bresser and Spiers (1997), the common feature of both
519 faults may be the high temperatures suggested by the activation of specific slip systems.

520 However, the experiments carried out by De Bresser and Spiers (1997) were performed at 3×10^5
521 s^{-1} and extrapolation of the results to higher strain rates should be undertaken with caution.

522 Combined numerical models and deformation experiments by Demurtas et al. (2019)
523 indicate that a temperature increase of approximately $\Delta T = 620 \text{ }^\circ\text{C}$ decays to about $50 \text{ }^\circ\text{C}$ over a
524 thermal diffusion distance of 2 mm inside carbonate fault gouge. Assuming a single shear-
525 heating event, the resulting temperature diffusion front could be captured as a change in
526 activated slip systems and associated CPOs. However, the absence of differences in slip systems
527 with decreasing temperature away from the PSS may suggest a later thermal overprint of the
528 cataclasite by more than one event. This overprint may lead to annealing of the microstructure
529 and a loss of an apparent temperature diffusion profile. Consequently, the analysed cataclasite
530 could contain several slip surfaces which are no longer discernible. The agreement between CPO
531 and subgrain misorientations suggests that crystal plasticity was the main deformation process to
532 produce the CPO rather than other, more exotic CPO-formation mechanisms such as surface
533 energy interactions (Toy *et al.*, 2015) or coupled solution and growth (Power and Tullis, 1989).
534 Overall, our results show that crystal plasticity played a role within the whole fault rock volume.

535 Water can have an influence on crystal-plastic deformation. It is known for quartz that a
536 higher water content can result in a transition of active slip systems from slip in the $\langle a \rangle$
537 directions to slip in the $[c]$ direction (Blacic, 1975) and a similar trend is observed by (Tokle *et*
538 *al.*, 2019) where added water can result in a different stress exponent. The temperature threshold
539 for the transition between different dislocation creep regimes in quartz can also be lowered by
540 about $100 \text{ }^\circ\text{C}$ by the addition of water (Hirth and Tullis, 1992). However, Stipp *et al.* (2002)
541 point out that the regimes identified by Hirth and Tullis (1992) may correspond to different types
542 of dynamic recrystallisation. The effect of water content on fabric transition is also known from

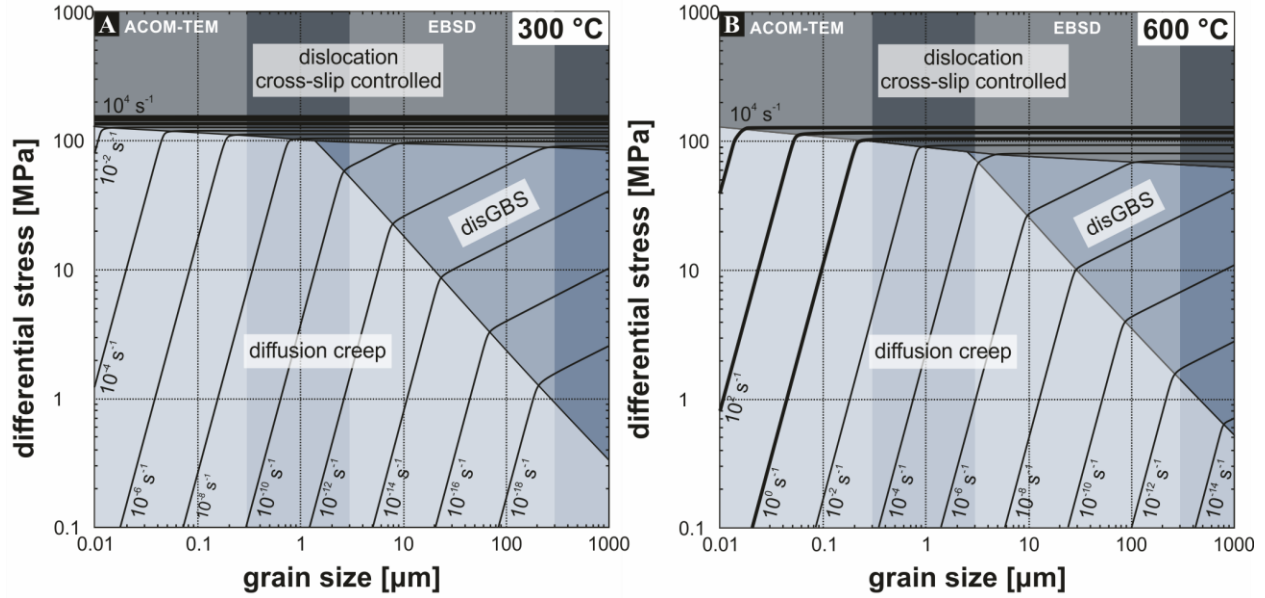
543 experiments on olivine where for example type-B ((010)[001]) and type-C ((100)[001]) CPOs
544 are more common with higher water content, whereas type-A ((010)[100]) is most common
545 without water (Jung and Karato, 2001). Deformation experiments on wet calcite at seismic
546 velocities show a stronger drop in friction coefficient compared to dry experiments (Chen *et al.*,
547 2017) and the development of a similar CPO to the one reported here (Demurtas *et al.*, 2019). It
548 has been inferred that the presence of water can promote hydrolytic weakening and influence
549 dislocation glide and climb in calcite (Liu *et al.*, 2002). We speculate that the above-mentioned
550 examples of water influencing crystal-plastic deformation may also have an influence on the
551 activity of specific glide systems and its activation temperature in crustal carbonate faults. The
552 addition of water could explain why De Bresser and Spiers (1997) consider the (c)<a> slip
553 system to be of minor importance because those experiments are performed dry and at low strain
554 rates. The involvement of water and its potential influence on crystal-plastic deformation
555 suggests that the proposed temperature range for the activation of (c)<a> (600–800 °C) and *r*-slip
556 (300–800 °C) may be different in other contexts. The influence of water on crystal plasticity in
557 calcite could be an alternative explanation why we do not observe a temperature gradient in
558 Figure 2 and 3, because no temperature gradient was produced. In such a case, the temperature
559 would evolve along the water-vapour transition as suggested by Chen *et al.* (2017).

560 The development of a CPO in natural carbonate faults has been reported before. For
561 example, (Smith *et al.*, 2013) and (Kim *et al.*, 2018) report a CPO and (Kim *et al.*, 2018)
562 speculate about the contribution of crystal plasticity during deformation. Our subgrain
563 misorientation analysis matches the inverse pole figures presented by displaying a rotational
564 maximum around [0001] close to the slip surface (Kim *et al.*, 2018). The intensity of the
565 maximum weakens over 10 cm away from the slip surface. This may indicate that temperature is

566 not the main governing factor for the activation of the (c)<a> glide system because temperature
567 diffusion would reach background values after about 2 mm (Demurtas *et al.*, 2019). In addition,
568 high dislocation densities are reported from numerous studies of natural faults, e.g. (Collettini *et*
569 *al.*, 2014). The study Collettini *et al.* (2014) shows free dislocations, as well as nanometric,
570 dislocation-free subgrains comparable to our observations in Figure 5.

571 **5.4 Deformation mechanism maps**

572 In the following, we will compare our microstructural observations and interpretations of
573 deformation mechanisms with theoretical considerations. We constructed deformation-
574 mechanism maps (DMMs) (Fig. 8) (Ashby, 1972) for both the approximate ambient temperature
575 conditions of 300 °C during the inter-seismic period at a depth of 3–5 km and the potential high-
576 temperature conditions of 600 °C attained by seismic shear heating, constrained by the observed
577 CPO and sp² hybridisation of partly-hybridised amorphous carbon (Ohl *et al.*, 2020). The
578 parameters for the flow laws utilised in Figure 8 are $A = 10^{7.63}$, $n = 1.1$, $p = 3.3$, $Q = 200 \text{ kJ mol}^{-1}$
579 for diffusion creep (Herwegh *et al.*, 2003); $A = 10^{4.93}$, $n = 1.67$, $p = 1.87$, $Q = 190 \text{ kJ mol}^{-1}$ for
580 disGBS (Walker *et al.*, 1990) and for cross-slip-controlled plasticity (De Bresser, 2002); where A
581 is a material-dependent factor, n is the stress exponent, p is the grain-size exponent, and Q is the
582 activation energy. As a first approximation, we only consider flow laws for materials with grain
583 sizes on the order of 10^{-8} – 10^{-3} m. We also investigated a flow law derived for water-assisted
584 grain-boundary diffusion modified by Verberne *et al.* (2019) and found that it produced the same
585 slope of strain rate contours but predicted lower strain rates than the flow law by Herwegh *et al.*,
586 (2003). Future investigations will also need to determine the impact of flow laws explicitly
587 derived for nanogranular materials (Mohamed, 2011).



588

589 *Figure 8: Deformation-mechanism maps for calcite at (A and C) 600 °C and (E and D) 300 °C. Light-shaded areas*
 590 *indicate the grain-size ranges from crystal orientation mapping by ACOM-TEM and EBSD. **A and B:** Deformation*
 591 *mechanism maps with three domains: diffusion creep (Herwegh *et al.*, 2003), disGBS (Walker *et al.*, 1990) and*
 592 *cross-slip controlled dislocation glide (De Bresser, 2002). Bold lines represent relevant strain rates.*
 593

594

595

Figure 8 displays DMMs calculated for temperatures of 300 °C and 600 °C representing

596 the onset of seismic slip and potential peak deformation conditions, respectively. The difference

597 in temperature has little influence on the position of the field boundaries but has a significant

598 impact on the predicted strain rates. The constraints on the grain sizes in this study are good, but

599 we lack reliable estimates of the stresses. At lower stresses, $\lesssim 100$ MPa, more typical of shallow

600 faults (e.g., Behr and Platt, 2014) the material is predicted to deform by diffusion creep and/or

601 disGBS, depending on grain size. Close to a field boundary, dislocation activity may contribute

602 to the total strain even within the diffusion creep field. Figure 8A suggests that at strain rates of $>$

603 1 s^{-1} and a temperature of 300 °C, approximating the onset of seismic slip, calcite would deform

604 by cross-slip controlled dislocation glide. Figure 8B indicates that at 600 °C diffusion creep

605 following the flow law of (Herwegh *et al.*, 2003) can accommodate a strain rate of $> 1 \text{ s}^{-1}$, in

606 material with grain sizes of < 100 nm at stresses < 10 MPa. At 600 °C, coseismic strain rates (1–

607 10^4 s^{-1}) can be accommodated in the PSS by either diffusion creep or plasticity depending on the
608 differential stress. In general, the DMMs predict that seismic strain rates could be accommodated
609 by cross-slip-controlled dislocation glide at stresses $>100 \text{ MPa}$.

610 We show that crystal-plasticity plays a role during the deformation of fault rocks within
611 the vicinity of principal slip surfaces. Although the DMMs in Figure 8 predict the operation of
612 deformation mechanisms known to not produce a strong CPO, our micro-, and nanostructural
613 observations indicate the activation of several slip systems resulting in CPO development. Future
614 studies need to further evaluate the competition between crystal plasticity and GBS processes
615 during the seismic cycle. The potential multitude of deformation processes operating within
616 natural faults and the comparison to predictions made by DMMs shows that extrapolating
617 experimentally derived flow laws to high-strain rate deformation may not be straightforward,
618 especially when conditions are close to a field boundary. However, a way of combining our
619 microstructural observations and the DMMs constructed here is by considering the operation of
620 different deformation mechanisms changing dynamically during the seismic cycle.

621

622 **5.5 Rheological considerations**

623 **5.5.1 Piezometric equilibrium and dynamic recrystallisation**

624 The analysis above indicates that crystal plasticity and grain annealing are feasible even
625 under upper-crustal conditions in the brittle regime. Nevertheless, crystal plasticity and GBS
626 processes will be cooperating mechanisms during fault rock deformation. To further decipher the
627 physical nature behind co-seismic deformation processes, Pozzi *et al.*, (2019) proposed the
628 establishment of a piezometric equilibrium during dynamic recrystallisation between GSI and
629 GSS deformation mechanisms. The authors propose that this equilibrium promotes rheological
630 weakening during seismic slip due to cycles of grain-size reduction and thermally driven grain

631 growth. We can further assess the piezometric relationship for recrystallised calcite grains with
632 the relation proposed by (Platt and De Bresser, 2017):

$$633 \quad D = K \sigma^{-p} \quad (3)$$

634 where D is the recrystallised grain size in μm , $K = 1243$, σ is the differential stress in MPa, and p
635 $= 1.09$. For the cataclasite region with grain sizes of approximately $5\text{--}2 \mu\text{m}$, Eqn. 3 predicts
636 differential stresses in the range $158\text{--}365$ MPa. For the foam nanostructure (Fig. 6) with grain
637 sizes of approximately $200\text{--}20$ nm, Eqn. 3 predicts differential stresses in the range $3\text{--}24$ GPa.
638 While the differential stresses for the cataclasite are plausible on a fault plane, the potential
639 differential stresses estimated for the foam nanostructure are implausibly high and demonstrate
640 that the piezometric relationship of Platt and De Bresser (2017), which was calibrated for much
641 coarser grain sizes, is not applicable in this context. Either the piezometric relationship has a
642 different slope at these finer grain sizes or the nanograins formed by mechanisms other than
643 dynamic recrystallisation.

644 **5.5.2 Post-seismic annealing and fault rock strength**

645 Our observations of the grain-boundary morphology within the Arkitsa nanostructure (Fig. 4C)
646 suggest that post-seismic annealing occurred via static recrystallization and grain growth through
647 grain-boundary migration. We define two foam nanostructures, old and new, depending on the
648 overprinting relationship. The older foam nanostructure lies at a greater distance from the PSS
649 (Fig. 4C, white circle), while the new foam nanostructure borders the PSS (Fig. 4C, black
650 circles). We interpret apparent linear discontinuities that displace grains (Fig. 4C) as fractures
651 originating from the PSS. These fractures cross-cut grains of the interlocked nanostructure
652 overprinting the old foam structure (Fig. 4C). Larger grains within the old foam nanostructure
653 (Fig. 4C, white circle) are truncated by fractures that cannot be traced back to the PSS but

654 terminate within the new foam nanostructure (Fig. 4C, black circle), instead. The resulting cross-
655 cutting relationships suggest fault reactivation after static recrystallisation. Angular relations
656 indicate that the fractures are Riedel shears (Verberne *et al.*, 2013) and suggest that slip along the
657 PSS may have also taken place during an advanced stage of nanostructural evolution.

658 To assess the influence of grain size on the strength of the PSZ, we calculate the required
659 minimum shear stress, σ_s , to fracture a grain of size d [m] using a modified Hall-Petch equation
660 (Sammis and Ben-Zion, 2008):

$$661 \quad \sigma_s = Y/2 = \frac{2 C K_{Ic}}{\sqrt{d}} \quad (4)$$

662 where $C = \sqrt{\frac{2}{3}}$ and $K_{Ic} = 0.39 \text{ MPa } \sqrt{m}$ (calcite, Broz *et al.*, 2006). For grain sizes of
663 approximately 5–2 μm , Eqn. 4 predicts minimum shear stresses in the range 285–450 MPa. For
664 the median grain size of 21 nm from ACOM-TEM, Eqn. 4 predicts a minimum shear stress of
665 4.4 GPa. Given the spread of the grain-size distribution, we also determine σ_s for a grain size of
666 200 nm (Figure 6A and B) and obtain 1.4 GPa. Based on these calculations, it is evident that
667 with decreasing grain size, slip localization onto the PSS increases because the required shear
668 stress to fracture grains increases. However, the modified Hall-Petch equation by (Sammis and
669 Ben-Zion, 2008) is derived from fitting empirical data from Al_2O_3 spheres and the value for K_{Ic} is
670 also empirically derived from microindentation which leads us to apply equation (4) with
671 caution. Alternatively, either local grain-scale stresses may be higher than the overall average
672 stress state of the fault during slip or fractures develop preferentially along zones of weakness,
673 such as cleavage and twin planes.

674 The localisation of slip can be observed over six orders of magnitude (μm – m) and
675 suggests a repeated toughening of the microstructure by grain-boundary strengthening. Our
676 microstructural observations coupled to DMM predictions suggest that at small grain sizes

677 diffusion creep and dislocation creep were active. Deformation by GBS would result in
678 stretching and elongation of the host-rock clasts (Figure 2A and 3A) but the initial shape of the
679 fragments is preserved despite showing an internal, polygonal structure expected to form by
680 GBS. This example is further illustrated by another clast in a transition stage consisting half of a
681 fine-grained microstructure and half of a single crystal. These examples show that the internal
682 structure is not diagnostic for GBS. Grain-size reduction by deformation and annealing suggests
683 that with evolving localisation the fault plane becomes progressively stronger with every
684 annealing step. This proposition supports the existence of a grain-boundary strengthening effect
685 within the fault rock volume. The inset in figure 1D shows the presence of a secondary slip
686 surface which develops inside the Schinos cataclasite. We propose that the formation of
687 additional slip surfaces is the first microscale evidence for the locking of the fault rock volume
688 immediately below the PSS. This interpretation is consistent with photographs of the fault
689 exposures (Fig. 1B and D) that show the development of new fault planes inside the wider fault
690 damage zone. Hence, the development of multiple slip surfaces may be the macroscopic
691 expression of a repeated grain-boundary strengthening effect. Ultimately, the grain size along the
692 fault plane may reach a critical limit, prompting the fault plane to jump and localise elsewhere
693 inside the damage zone leading to the formation of multiple slip surfaces.

694 **6 Conclusion**

695 The subgrain misorientations and the matching crystallographic preferred orientations across
696 different scales indicate that crystal plasticity played a role during fault rock formation. Although
697 the precise nature of slip systems at sub-seismic velocities are unknown, our results may suggest
698 that the slip systems inferred from subgrain misorientation analysis are potentially indicative of
699 high temperatures during co-seismic deformation or the influence of water. Nevertheless, future

700 studies need to further evaluate the applicability of slip-system analyses as paleoseismicity
701 indicators, especially comparing dry and wet deformation. Plastic straining and tempering,
702 described as cold working and annealing, offers an alternative mechanism to produce a cohesive
703 nanogranular material. Paleopiezometric estimations based on grain sizes immediately below the
704 slip surface suggest that either dynamic recrystallization did not take place or at least did not
705 follow the piezometer calibrated by low-strain rate experiments. The cyclic repetition of plastic
706 strain, annealing and static recrystallization via grain-boundary migration produces a grain-
707 boundary strengthening effect until the grain size reaches a critical minimum. This strengthening
708 effect forces the fault plane to relocate inside the fault damage zone, resetting the deformation
709 cycle.

710 Acknowledgements

711 This study was funded by the Dutch research organisation (NWO) with the project number
712 ALWOP.2015.082. O.P. is supported by an ERC starting grant “nanoEARTH” (852069). The
713 authors also thank Edgar Rauch for discussion and input regarding ACOM-TEM, A. Niemeijer,
714 E. Korkolis and J.H.P. De Bresser for discussions and I. Koukouvelas. The TEM facility in Lille
715 (France) is supported by the Conseil Regional du Nord-Pas de Calais, and the European Regional
716 Development Fund (ERDF).

717 Data availability

718 All datasets found in this manuscript will be made available open access through the European
719 Plate Observing System at <https://public.yoda.uu.nl/geo/UU01/A77O7X.html>.

720 References

- 721 Ambraseys, N. N. and Jackson, J. A. (1990) 'Seismicity and associated strain of central Greece
722 between 1890 and 1988', *Geophysical Journal International*, pp. 663–708. doi:
723 10.1111/j.1365-246x.1990.tb05577.x.
- 724 Ashby, M. F. (1972) 'A first report on deformation-mechanism maps', *Acta Metallurgica*, pp.
725 887–897. doi: 10.1016/0001-6160(72)90082-x.
- 726 Bachmann, F., Hielscher, R. and Schaeben, H. (2011) 'Grain detection from 2d and 3d EBSD
727 data—Specification of the MTEX algorithm', *Ultramicroscopy*, pp. 1720–1733. doi:
728 10.1016/j.ultramic.2011.08.002.
- 729 Barnhoorn, A. et al. (2005) 'Post-deformational annealing of calcite rocks', *Tectonophysics*, pp.
730 167–191. doi: 10.1016/j.tecto.2005.04.008.
- 731 Behr, W. M. and Platt, J. P. (2014) 'Brittle faults are weak, yet the ductile middle crust is strong:
732 Implications for lithospheric mechanics', *Geophysical Research Letters*, pp. 8067–8075.
733 doi: 10.1002/2014gl061349.
- 734 Blacic, J. D. (1975) 'Plastic-deformation mechanisms in quartz: The effect of water',
735 *Tectonophysics*, pp. 271–294. doi: 10.1016/0040-1951(75)90021-9.
- 736 Blenkinsop, T. G. (1991) 'Cataclasis and processes of particle size reduction', *Pure and Applied*
737 *Geophysics PAGEOPH*, pp. 59–86. doi: 10.1007/bf00878888.
- 738 Broz, M. E., Cook, R. F., Whitney D. L 'Microhardness, toughness, and modulus of Mohs scale
739 minerals', *American Mineralogist*, 91 (1): 135–142. doi: doi: 10.2138/am.2006.1844
- 740 Bürgmann, R. and Dresen, G. (2008) 'Rheology of the Lower Crust and Upper Mantle: Evidence
741 from Rock Mechanics, Geodesy, and Field Observations', *Annual Review of Earth and*
742 *Planetary Sciences*, pp. 531–567. doi: 10.1146/annurev.earth.36.031207.124326.
- 743 Chen, J. et al. (2017) 'Water vaporization promotes coseismic fluid pressurization and buffers
744 temperature rise', *Geophysical Research Letters*, pp. 2177–2185. doi:
745 10.1002/2016gl071932.
- 746 Collettini, C. et al. (2014) 'Fault structure and slip localization in carbonate-bearing normal
747 faults: An example from the Northern Apennines of Italy', *Journal of Structural Geology*,
748 pp. 154–166. doi: 10.1016/j.jsg.2014.07.017.
- 749 Collier, R. E. L. et al. (1998) 'Paleoseismicity of the 1981 Corinth earthquake fault: Seismic
750 contribution to extensional strain in central Greece and implications for seismic hazard',
751 *Journal of Geophysical Research: Solid Earth*, pp. 30001–30019. doi: 10.1029/98jb02643.
- 752 Covey-Crump, S. J. (1997) 'The normal grain growth behaviour of nominally pure calcitic
753 aggregates', *Contributions to Mineralogy and Petrology*, pp. 239–254. doi:

- 754 10.1007/s004100050335.
- 755 De Bresser, J. H. P. (2002) ‘On the mechanism of dislocation creep of calcite at high
756 temperature: Inferences from experimentally measured pressure sensitivity and strain rate
757 sensitivity of flow stress’, *Journal of Geophysical Research: Solid Earth*, p. ECV 4–1. doi:
758 10.1029/2002jb001812.
- 759 De Bresser, J. H. P. and Spiers, C. J. (1997) ‘Strength characteristics of the r, f, and c slip
760 systems in calcite’, *Tectonophysics*, 272(1), pp. 1–23. doi: 10.1016/S0040-1951(96)00273-
761 9.
- 762 Delle Piane, C. et al. (2017) ‘Generation of amorphous carbon and crystallographic texture
763 during low-temperature subseismic slip in calcite fault gouge’, *Geology*, pp. 163–166. doi:
764 10.1130/g39584.1.
- 765 Demurtas, M. et al. (2019) ‘Development of crystallographic preferred orientation during
766 cataclasis in low-temperature carbonate fault gouge’, *Journal of Structural Geology*, pp. 37–
767 50. doi: 10.1016/j.jsg.2019.04.015.
- 768 De Paola, N. et al. (2015) ‘Can grain size sensitive flow lubricate faults during the initial stages
769 of earthquake propagation?’, *Earth and Planetary Science Letters*, pp. 48–58. doi:
770 10.1016/j.epsl.2015.09.002.
- 771 Di Toro, G. et al. (2011) ‘Fault lubrication during earthquakes’, *Nature*, 471(7339), pp. 494–498.
772 doi: 10.1038/nature09838.
- 773 Druiventak, A. et al. (2012) ‘Kick-and-cook experiments on peridotite: simulating coseismic
774 deformation and post-seismic creep’, *Terra Nova*, 24(1), pp. 62–69. doi: 10.1111/j.1365-
775 3121.2011.01038.x
- 776 Ferraro, F. et al. (2018) ‘Space-time evolution of cataclasis in carbonate fault zones’, *Journal of*
777 *Structural Geology*, pp. 45–64. doi: 10.1016/j.jsg.2018.02.007.
- 778 Hansen, L. N., Zimmerman, M. E. and Kohlstedt, D. L. (2011) ‘Grain boundary sliding in San
779 Carlos olivine: Flow law parameters and crystallographic-preferred orientation’, *Journal of*
780 *Geophysical Research*. doi: 10.1029/2011jb008220.
- 781 Heilbronner, R. and Barrett, S. (2014) ‘Fractal Grain Size Distributions’, in Heilbronner, R. and
782 Barrett, S. (eds) *Image Analysis in Earth Sciences*. Berlin, Heidelberg: Springer Berlin
783 Heidelberg, pp. 225–249.
- 784 Herwegh, M., Xiao, X. and Evans, B. (2003) ‘The effect of dissolved magnesium on diffusion
785 creep in calcite’, *Earth and Planetary Science Letters*, pp. 457–470. doi: 10.1016/s0012-
786 821x(03)00284-x.
- 787 Hielscher, R. and Schaeben, H. (2008) ‘A novel pole figure inversion method: specification of
788 theMTEXalgorithm’, *Journal of Applied Crystallography*, pp. 1024–1037. doi:
789 10.1107/s0021889808030112.

- 790 Hirth, G. and Kohlstedt, D. L. (1995) ‘Experimental constraints on the dynamics of the partially
791 molten upper mantle: Deformation in the diffusion creep regime’, *Journal of Geophysical*
792 *Research: Solid Earth*, pp. 1981–2001. doi: 10.1029/94jb02128.
- 793 Hirth, G. and Tullis, J. (1992) ‘Dislocation creep regimes in quartz aggregates’, *Journal of*
794 *Structural Geology*, pp. 145–159. doi: 10.1016/0191-8141(92)90053-y.
- 795 Hollandt, J. et al. (2010) ‘Industrial Applications of Radiation Thermometry’, in *Radiometric*
796 *Temperature Measurements: II. Applications*. Elsevier (Experimental Methods in the
797 *Physical Sciences*), pp. 1–56.
- 798 Humphreys, F. J. and Hatherly, M. (2004) *Recrystallization and Related Annealing Phenomena*.
799 Elsevier.
- 800 Jung, H. and Karato S (2001) ‘Water-induced fabric transitions in olivine’, *Science*, 293(5534),
801 pp. 1460–1463. doi: 10.1126/science.1062235.
- 802 Kaplanis, A. et al. (2013) ‘Kinematics and Ophiolite obduction in the Gerania and Helicon
803 Mountains, central Greece’, *Tectonophysics*, pp. 215–234. doi: 10.1016/j.tecto.2012.07.014.
- 804 Keulen, N. et al. (2007) ‘Grain size distributions of fault rocks: A comparison between
805 experimentally and naturally deformed granitoids’, *Journal of Structural Geology*, pp.
806 1282–1300. doi: 10.1016/j.jsg.2007.04.003.
- 807 Kim, S. et al. (2018) ‘Fabric transition with dislocation creep of a carbonate fault zone in the
808 brittle regime’, *Tectonophysics*, pp. 107–116. doi: 10.1016/j.tecto.2017.12.008.
- 809 Kokkalas, S. et al. (2007) ‘Quantitative fault analysis at Arkitsa, Central Greece, using
810 Terrestrial Laser- Scanning (“LIDAR”)’, *Bulletin of the Geological Society of Greece*, p.
811 1959. doi: 10.12681/bgsg.17237.
- 812 Komura, S. et al. (2001) ‘An evaluation of the flow behavior during high strain rate
813 superplasticity in an Al-Mg-Sc alloy’, *Metallurgical and Materials Transactions A*, pp. 707–
814 716. doi: 10.1007/s11661-001-0087-9.
- 815 Kumar, K. S. et al. (2003) ‘Deformation of electrodeposited nanocrystalline nickel’, *Acta*
816 *Materialia*, pp. 387–405. doi: 10.1016/s1359-6454(02)00421-4.
- 817 Lambrakis, N., Katsanou, K. and Siavalas, G. (2014) ‘Chapter 3: Geothermal fields and thermal
818 waters of Greece: an overview’, in Baba, A., Bundschuh, J., and D., C. (eds) *Geothermal*
819 *Systems and Energy Resources: Turkey and Greece*. CRC Press (1st), pp. 25–45.
- 820 Langdon, T. G. (2006) ‘Grain boundary sliding revisited: Developments in sliding over four
821 decades’, *Journal of Materials Science*, pp. 597–609. doi: 10.1007/s10853-006-6476-0.
- 822 Liu, J., Walter, J. M. and Weber, K. (2002) ‘Fluid-enhanced low-temperature plasticity of calcite
823 marble: Microstructures and mechanisms’, *Geology*. doi:10.1130/0091-7613(2002)030<0787:
824 FELTPO>2.0.CO;2.

- 825 Lu, L., Sui, M. L. and Lu, K. (2000) 'Superplastic extensibility of nanocrystalline copper at room
826 temperature', *Science*, 287(5457), pp. 1463–1466. doi: 10.1126/science.287.5457.1463.
- 827 Ma, E. (2004) 'Watching the nanograins roll', *Science*, pp. 623–624. doi:
828 10.1126/science.1101589.
- 829 Matysiak, A. K. and Trepmann, C. A. (2012) 'Crystal–plastic deformation and recrystallization
830 of peridotite controlled by the seismic cycle', *Tectonophysics*, 530-531, pp. 111–127. doi:
831 10.1016/j.tecto.2011.11.029.
- 832 Mendrinou, D. et al. (2010) 'Exploring for geothermal resources in Greece', *Geothermics*, pp.
833 124–137. doi: 10.1016/j.geothermics.2009.11.002.
- 834 Metaxas, A. et al. (2010) 'Geothermic status of Thermopylae - Anthili area in Fthiotida
835 prefecture', *Bulletin of the Geological Society of Greece*, p. 2265. doi:
836 10.12681/bgsg.11426.
- 837 Mohamed, F. A. (2011) 'Deformation mechanism maps for micro-grained, ultrafine-grained, and
838 nano-grained materials', *Materials Science and Engineering: A*, pp. 1431–1435. doi:
839 10.1016/j.msea.2010.10.048.
- 840 Nielsen, S. (2017) 'From slow to fast faulting: recent challenges in earthquake fault mechanics',
841 *Philosophical transactions. Series A, Mathematical, physical, and engineering sciences*,
842 375(2103). doi: 10.1098/rsta.2016.0016.
- 843 Niemeijer, A. et al. (2012) 'Inferring earthquake physics and chemistry using an integrated field
844 and laboratory approach', *Journal of Structural Geology*, pp. 2–36. doi:
845 10.1016/j.jsg.2012.02.018.
- 846 Papachristou, M. et al. (2014) 'Chapter 4: Geological setting, geothermal conditions and
847 hydrochemistry of south and southeastern Aegean geothermal systems', in Baba, A.,
848 Bundschuh, J., and D., C. (eds) *Geothermal Systems and Energy Resources: Turkey and
849 Greece*. CRC Press (1st), pp. 47–75.
- 850 Papoulis, D. et al. (2013) 'Clay minerals from the Arkitsa fault gouge zone, in Central Greece,
851 and implications for fluid flow', *Bulletin of the Geological Society of Greece*, pp. 616–624.
852 doi: 10.12681/bgsg.11095.
- 853 Pieri, M. et al. (2001) 'Rheological and microstructural evolution of Carrara marble with high
854 shear strain: results from high temperature torsion experiments', *Journal of Structural
855 Geology*, pp. 1393–1413. doi: 10.1016/s0191-8141(01)00006-2.
- 856 Platt, J. P. and De Bresser, J. H. P. (2017) 'Stress dependence of microstructures in
857 experimentally deformed calcite', *Journal of Structural Geology*, pp. 80–87. doi:
858 10.1016/j.jsg.2017.10.012.
- 859 Power, W. L. and Tullis, T. E. (1989) 'The relationship between slickenside surfaces in fine-
860 grained quartz and the seismic cycle', *Journal of Structural Geology*, pp. 879–893. doi:

- 861 10.1016/0191-8141(89)90105-3.
- 862 Pozzi, G. et al. (2019) ‘Coseismic ultramylonites: An investigation of nanoscale viscous flow
863 and fault weakening during seismic slip’, *Earth and Planetary Science Letters*, pp. 164–175.
864 doi: 10.1016/j.epsl.2019.03.042.
- 865 Rauch, E. F. and Véron, M. (2014) ‘Automated crystal orientation and phase mapping in TEM’,
866 *Materials Characterization*, pp. 1–9. doi: 10.1016/j.matchar.2014.08.010.
- 867 Renner, J., Evans, B. and Siddiqi, G. (2002) ‘Dislocation creep of calcite’, *Journal of*
868 *Geophysical Research: Solid Earth*, p. ECV 6–1. doi: 10.1029/2001jb001680.
- 869 Rice, J. R. (2006) ‘Heating and weakening of faults during earthquake slip’, *Journal of*
870 *Geophysical Research: Solid Earth*. doi: 10.1029/2005jb004006.
- 871 Rutter, E. H., Casey, M. and Burlini, L. (1994) ‘Preferred crystallographic orientation
872 development during the plastic and superplastic flow of calcite rocks’, *Journal of Structural*
873 *Geology*, pp. 1431–1446. doi: 10.1016/0191-8141(94)90007-8.
- 874 Sammis, C. G. et al. (1986) ‘Self-similar cataclasis in the formation of fault gouge’, *Pure and*
875 *Applied Geophysics PAGEOPH*, pp. 53–78. doi: 10.1007/bf00875719.
- 876 Sammis, C. G. and Ben-Zion, Y. (2008) ‘Mechanics of grain-size reduction in fault zones’,
877 *Journal of geophysical research*, 113(B2), p. 553. doi: 10.1029/2006JB004892.
- 878 Sammis, C., King, G. and Biegel, R. (1987) ‘The kinematics of gouge deformation’, *Pure and*
879 *Applied Geophysics PAGEOPH*, pp. 777–812. doi: 10.1007/bf00878033.
- 880 Schmid, S. M., Boland, J. N. and Paterson, M. S. (1977) ‘Superplastic flow in finegrained
881 limestone’, *Tectonophysics*, pp. 257–291. doi: 10.1016/0040-1951(77)90120-2.
- 882 Scholz, C. H. (1988) ‘The brittle-plastic transition and the depth of seismic faulting’,
883 *Geologische Rundschau*, pp. 319–328. doi: 10.1007/bf01848693.
- 884 Scholz, C. H. (1998) ‘Earthquakes and friction laws’, *Nature*, 391(6662), pp. 37–42. doi:
885 10.1038/34097.
- 886 Sibson, R. (1982) ‘Fault zone models, heat flow, and the depth distribution of earthquakes in the
887 continental crust of the United States’, *Bulletin of the Seismological Society of America*,
888 72(1), pp. 151–163.
- 889 Smith, S. A. F. et al. (2013) ‘Coseismic recrystallization during shallow earthquake slip’,
890 *Geology*, pp. 63–66. doi: 10.1130/g33588.1.
- 891 Stipp, M. et al. (2002) ‘The eastern Tonale fault zone: a “natural laboratory” for crystal plastic
892 deformation of quartz over a temperature range from 250 to 700°C’, *Journal of Structural*
893 *Geology*, pp. 1861–1884. doi: 10.1016/s0191-8141(02)00035-4.

- 894 Thomson, S. N., Stöckhert, B. and Brix, M. R. (1998) 'Thermochronology of the high-pressure
895 metamorphic rocks of Crete, Greece: Implications for the speed of tectonic processes',
896 *Geology*, p. 259. doi: 10.1130/0091-7613(1998)026<0259:tothpm>2.3.co;2.
- 897 Tokle, L., Hirth, G. and Behr, W. M. (2019) 'Flow laws and fabric transitions in wet quartzite',
898 *Earth and planetary science letters*, 505, pp. 152–161. doi: 10.1016/j.epsl.2018.10.017.
- 899 Toy, V. G. et al. (2015) 'Crystallographic preferred orientations may develop in nanocrystalline
900 materials on fault planes due to surface energy interactions', *Geochemistry, Geophysics,*
901 *Geosystems*, pp. 2549–2563. doi: 10.1002/2015gc005857.
- 902 Trepmann, C. A. et al. (2017) 'Recrystallization of quartz after low-temperature plasticity – The
903 record of stress relaxation below the seismogenic zone', *Journal of Structural Geology*, 95,
904 pp. 77–92. doi: 10.1016/j.jsg.2016.12.004.
- 905 Trepmann, C. A. and Stöckhert, B. (2013) 'Short-wavelength undulatory extinction in quartz
906 recording coseismic deformation in the middle crust – an experimental study', *Solid Earth*,
907 pp. 263–276. doi: 10.5194/se-4-263-2013.
- 908 Verberne, B. A. et al. (2013) 'Nanocrystalline slip zones in calcite fault gouge show intense
909 crystallographic preferred orientation: Crystal plasticity at sub-seismic slip rates at 18–150
910 °C', *Geology*, pp. 863–866. doi: 10.1130/g34279.1.
- 911 Verberne, B. A., Plümper, O. and Spiers, C. J. (2019) 'Nanocrystalline Principal Slip Zones and
912 Their Role in Controlling Crustal Fault Rheology', *Minerals*, p. 328. doi:
913 10.3390/min9060328.
- 914 Walker, A. N., Rutter, E. H. and Brodie, K. H. (1990) 'Experimental study of grain-size sensitive
915 flow of synthetic, hot-pressed calcite rocks', *Geological Society, London, Special*
916 *Publications*, pp. 259–284. doi: 10.1144/gsl.sp.1990.054.01.24.
- 917